PHYSICAL SCIENCE

Direct observation of chiral currents and magnetic reflection in atomic flux lattices

Fangzhao Alex An, Eric J. Meier, Bryce Gadway*

The prospect of studying topological matter with the precision and control of atomic physics has driven the development of many techniques for engineering artificial magnetic fields and spin-orbit interactions. Recently, the idea of introducing nontrivial topology through the use of internal (or external) atomic states as effective "synthetic dimensions" has garnered attraction for its versatility and possible immunity from heating. We engineer tunable gauge fields through the local control of tunneling phases in an effective two-dimensional manifold of discrete atomic momentum states. We demonstrate the ability to create homogeneous gauge fields of arbitrary value, directly imaging the site-resolved dynamics of induced chiral currents. Furthermore, we engineer the first inhomogeneous artificial gauge fields for cold atoms, observing the magnetic reflection of atoms incident upon a step-like variation of an artificial vector potential. These results open new possibilities for the study of topological phases and localization phenomena in atomic gases.

INTRODUCTION

The purity and microscopic understanding of ultracold atomic matter have made it an ideal platform for the study of topological phenomena (*1*). In addition, the high level of control over atomic systems has enabled the exploration of topological phases not readily accessible in real materials. The past decade has seen steady progress toward the realization of stable, low-temperature atomic samples with nontrivial topology. Lattice-based techniques using lattice modulation (*2*–*4*) and laser addressing (*5*–*7*) have proven capable of reaching the regimes of large effective magnetic fields and strong spin-orbit coupling, a feat that has eluded bulk gas techniques, such as rotation (*8*) and bulk Raman addressing (*9*–*11*). Still, nontrivial heating remains an issue for lattice-based schemes (*12*, *13*).

Recently, the use of atomic internal states as synthetic dimensions (*14*–*18*) has emerged as an interesting alternative strategy that may obviate some sources of heating. Although various analogs of real-space transport have previously been studied (*19*–*22*), the application of spectroscopically controlled, field-driven transitions has led to recent key developments, including the realization of two-dimensional (2D) systems with fixed artificial flux (*16*, *17*).

Here, we expand the capabilities of synthetic dimension–based simulation by engineering fully tunable flux lattices in multiple synthetic dimensions. We directly image chiral atomic currents induced by a homogeneous flux and observe magnetic reflection of atoms from a step-like jump of an effective magnetic vector potential generated by an inhomogeneous flux. These advances in the creation of artificial gauge fields should greatly expand the variety of topological systems open to investigation through cold-atom simulation.

Our implementation (*23*–*25*) laser couples the discrete momentum states of ultracold ^{87}Rb atoms to mimic tunnel-coupled lattice sites. In one dimension, we drive the two-photon Bragg transitions coupling these momentum states using counterpropagating laser fields with a wavelength λ_2 of 1064 nm (wave number $k_2 = 2\pi/\lambda_2$). Here, we extend this scheme to higher dimensions by adding a second set of Bragg laser beams (shown in Fig. 1A), copropagating and having an incommensurate wavelength (λ_1 = 781.5 nm, $k_1 = 2\pi/\lambda_1$) with respect to the λ_2 laser. The wave vectors $k_{1,2}$ define an effective 2D manifold of discrete momentum states carrying momentum $p_{m,n} = 2\hbar(mk_1 + nk_2)$ (depicted in Fig. 1B on top of the free-particle dispersion relation). Starting with a Bose-Einstein condensate at rest, we populate these states by applying m and n two-photon Bragg transitions from the k_1 and k_2 lasers, respectively. This mapping between the atoms' 1D momentum distribution and the 2D lattice with site indices (m, n) is depicted with sample data in Fig. 1 (C and D). By imprinting a multi-frequency spectrum onto each pair of lasers, we individually address every allowed transition in our fully synthetic 2D ladder system (Fig. 1E) with spectroscopic precision, allowing for full control of all tunneling terms and site energies (see the Supplementary Materials for more details).

RESULTS AND DISCUSSION

Chiral currents in the homogeneous flux ladder

We begin by directly mimicking a magnetic vector potential in the Landau gauge, $\hat{\mathbf{A}} = (0, Bx, 0)$, through coordination of the tunneling phases on a 2 × 5 site ladder. This gives rise to a uniform effective magnetic field, as shown in Fig. 2A. The dynamics of our cold atoms are effectively governed by the Hamiltonian

$$\hat{H} = -[t_x \sum_n \hat{c}^\dagger_{1,n}\hat{c}_{0,n} + t_y \sum_{m,n} e^{i\phi_{m,n}}\hat{c}^\dagger_{m,n+1}\hat{c}_{m,n}] + \text{h.c.} \quad (1)$$

where $\hat{c}_{m,n}$ ($\hat{c}^\dagger_{m,n}$) is the bosonic annihilation (creation) operator for the state with indices (m, n). In terms of the effective magnetic field strength B, the engineered tunneling phases along y are given by $\phi_{m,n} = -m\phi$, where $\phi = 2\pi d^2 B(q/hc)$ is the flux associated with closed loops around individual four-site plaquettes, d is the effective spacing between synthetic lattice sites, q is the effective charge of the particles, h is the Planck constant, and c is the speed of light. Here, and in the remainder of this work, we use approximately homogeneous tunneling strengths and engineer hard-wall (open) system boundaries.

To probe the influence of our tunable field B on these "charged" particles, we observe their nonequilibrium response to a quench of the effective field. In particular, we study the response of atoms initially

Department of Physics, University of Illinois at Urbana-Champaign, Urbana, IL 61801, USA.
*Corresponding author. Email: bgadway@illinois.edu

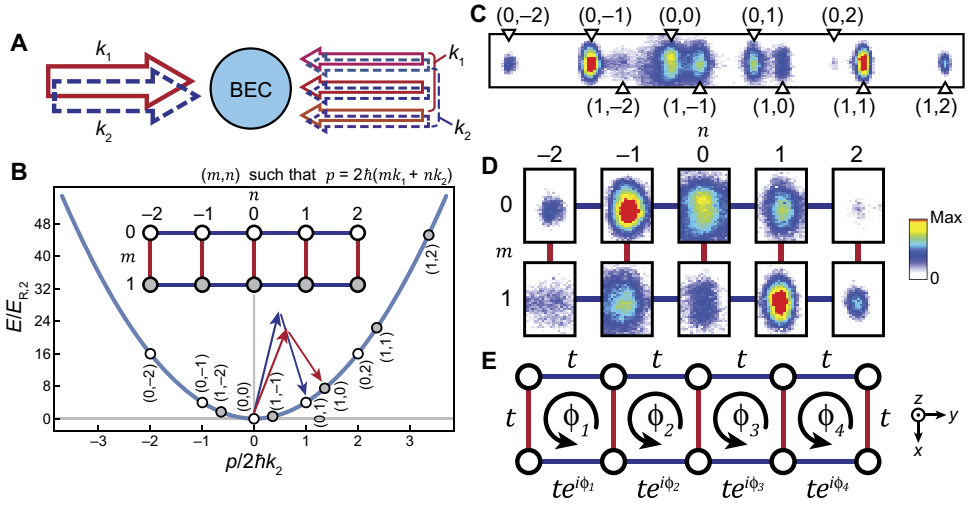

Fig. 1. Two-leg flux ladder. (**A**) Two sets of lattice laser fields (with wave numbers k_1 and k_2) addressing transitions between atomic momentum states of a Bose-Einstein condensate (BEC). (**B**) Free-particle dispersion relation showing momentum states on the $m = 0$ (white circles) and $m = 1$ (gray circles) legs, labeled by (m, n) with momentum $p = 2\hbar(mk_1 + nk_2)$. Short red and tall blue arrows denote transitions controlled by k_1 and k_2 wave number lattices, respectively. Inset: 2D lattice representation, with links addressed by the k_1 (red, vertical) and k_2 (blue, horizontal) wave number beams. The recoil energy is given by $E_{R,2} = \hbar^2 k_2^2 / 2M_{Rb}$. (**C**) Time-of-flight image of atoms in momentum orders (m, n). (**D**) Image from (C) rearranged to show the 2D lattice. This figure and (C) show absorption images using the normalized OD scale at the right. (**E**) Schematic of a two-leg ladder with applied tunneling phases ϕ_i on each link of the $m = 1$ leg, resulting in fluxes ϕ_i around each four-site plaquette. Max, maximum.

prepared in a symmetric superposition of occupation on sites (0, 0) and (1, 0). Because of the lack of interior lattice sites, this two-leg ladder geometry does not host the same bulk localization and conductance at the boundary typical of the integer quantum Hall effect. However, as depicted in Fig. 2A, the applied fluxes lead to anisotropically conducting chiral currents or a "shearing" of the initial symmetric state along the $m = 0$ and $m = 1$ legs. We define this shearing as

$$\text{shearing} \equiv \langle n \rangle_0 - \langle n \rangle_1 \tag{2}$$

where $\langle n \rangle_{0(1)}$ is the average site index along the $m = 0$ ($m = 1$) leg. In general, application of a positive flux ϕ will induce a clockwise chiral current and a positive shear, as shown in Fig. 2A. A sign reversal of the flux should result in a reversal of the shearing direction, and, for fluxes of zero or $\pm\pi$, we expect only symmetric spreading of the initial state along the y direction. Although recent experiments (*16*, *17*, *26*) have observed chiral currents on similar ladder geometries, our use of a fully synthetic lattice allows us to engineer arbitrary fluxes and, furthermore, enables direct observation of all site populations and shearing dynamics at the site-resolved level.

Figure 2B shows the observed shearing dynamics for applied fluxes $\phi = -\pi/2$ (top, violet) and $\phi = +\pi/2$ (bottom, red). Initially, all of the population resides in the middle sites and thus should give zero shear (see the Supplementary Materials regarding the small initial nonzero shear). The atoms thus follow the general trend described above: Positive flux causes atoms to move clockwise around the ladder, and negative flux leads to motion in the opposite direction. Because of the finite system size, the value of the shearing saturates and decreases, as the atoms reach the ends of the ladder and move between the two legs. Figure 2C shows the population distributions after a quench duration of 500 μs (dashed vertical lines in Fig. 2B) for fluxes $\phi = \pm\pi/2$. A clear distinction between the cases of positive and negative fluxes can be seen at this time, corresponding to the case of near-maximum shear. For longer times (as seen in Fig. 2B), the data tend to deviate from the simple theory simulations. The dashed curves are the predictions of Eq. 1 for a tunneling rate $t/\hbar = 2\pi \times 338$ Hz, which exceeds the calibrated tunneling rates in Fig. 2 (B and D) by ~25 and ~31%, respectively. Solid curves represent a more detailed model, including the influence of off-resonant Bragg transitions [(*23*); see Supplementary Text], but still ignoring the influences of interactions, finite condensate size, and decoherence due to both the phase instability of the Bragg lasers and the physical separation of wave packets with different momenta.

Figure 2D shows the measured shearing after 500 μs for the full range of applied flux values, demonstrating our wide control over homogeneous effective fields. Although almost no shear is measured for $\phi = 0$ (corresponding to symmetric spreading along y), maximum shearing magnitudes are observed for flux values near $\pm\pi/2$. The data are in excellent qualitative agreement with the theory curve, which has been scaled by a factor of 0.45 to account for reductions of shearing due to decoherence and other influences. Most of the deviations from the idealized dynamics of Eq. 1, including the small, nonzero shear for zero flux, are reproduced by this theory, accounting for residual off-resonant Bragg couplings [(*23*); see Supplementary Text]. Our complete control of flux values is a necessary step toward measurement of the Hofstadter spectrum in cold atoms (*5*).

Reflection from a magnetic defect

As a second study, we engineer the first inhomogeneous artificial gauge fields in cold atoms, studying the transport of atomic wave packets incident upon a sharp dislocation of the effective magnetic field. As shown in Fig. 3A, we engineer a step-like jump of the magnetic vector potential $\hat{\mathbf{A}}$ by fixing the flux in the leftmost plaquette to zero while retaining a tunable homogeneous flux ϕ in the remaining plaquettes. Without any initialization procedure, we begin with all of the population in the corner of the flux-free region on the zero momentum site (0, 0). By switching our couplings along y to the range $n = 0$ to $n = 4$, we shift the lattice such

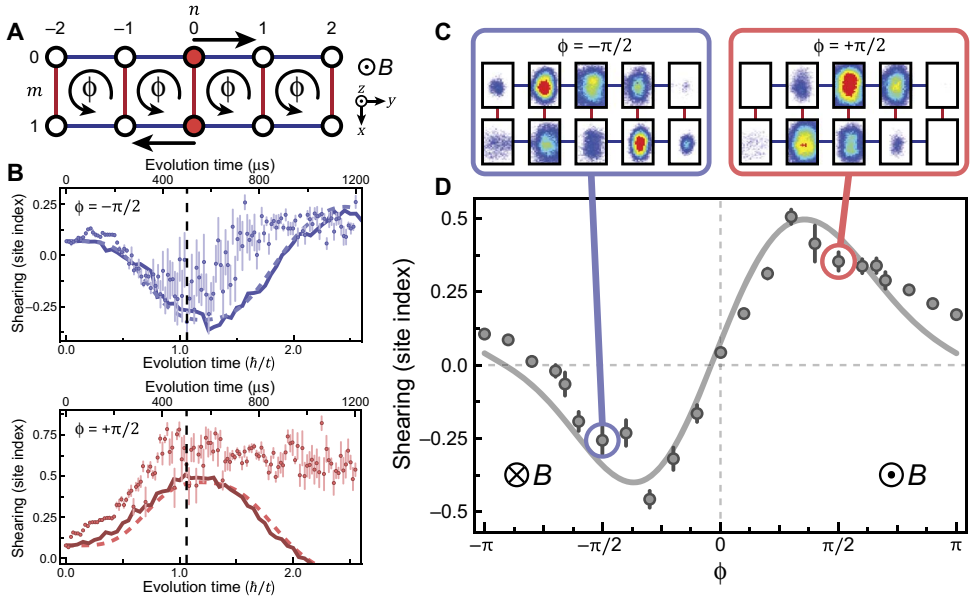

Fig. 2. Shearing in the flux ladder. (**A**) Schematic showing atoms undergoing clockwise shear (arrows) for positive flux ϕ, corresponding to an effective magnetic field B directed out of the page. Red filled-in circles represent the initial state. (**B**) Shearing dynamics for $\phi = -\pi/2$ (top, blue) and $\phi = +\pi/2$ (bottom, red). Dashed and solid curves represent numerical simulation results based on Eq. 1 and a more complete model taking into account off-resonant transitions, respectively, both scaled and offset to match the data. Dashed vertical lines indicate the time when the data for (C) and (D) were taken. (**C**) Site populations for $\phi = -\pi/2$ (left, blue) and $\phi = +\pi/2$ (right, red). Color scale used is the same as in Fig. 1D. (**D**) Shearing versus applied flux. Solid line represents results from a simulation of the more complete model. Measurements for (C) and (D) were taken after 500 μs (~1.06 $\hbar/t$), indicated by dashed vertical lines in (B). The calibrated tunneling rates for (B) and (D) are slightly different, so this time translates into different tunneling times for the two. All error bars denote 1 SE.

that atoms with zero momentum naturally start on the corner site. We quench on tunneling and the full flux distribution and track the dynamics of the atomic distributions, monitoring the percentage of atoms that transmit through the step-like boundary, escaping the leftmost four-site plaquette.

As shown in Fig. 3B, we probe the full range of ϕ, directly measuring the transmitted fraction of atoms after an evolution time of 1500 μs (~2.94 $\hbar/t$). The tunneling rate $t/\hbar = 2\pi \times 311(14)$ Hz has been determined from calibrations to two-site Rabi oscillations. A clear trend is observed: maximum transmission near $\phi = 0$, where the step in the vector potential vanishes, and maximum reflection for flux dislocations of $\pm\pi$. This is in good qualitative agreement with the predictions of the idealized tight-binding Hamiltonian of Eq. 1 (shown as green solid line in Fig. 3B). Note that this behavior is purely due to the presence of a flux boundary in this 2D system and is not observed in the limit of zero interleg tunneling, where there are no relevant flux loops. Specifically, for corresponding data taken on a 1D chain with a step-like tunneling phase boundary, no reflection is observed.

Although the idealized predictions of Eq. 1 expect full transmission for $\phi = 0$ (and roughly 40% for $\phi = \pm\pi$), we observe reduced dynamics in the data, which we attribute to experimental sources of decoherence and dephasing that may be ameliorated in future investigations (see Supplementary Text). Moreover, we find that a sizable fraction of the atoms in our initial condensate [site (0, 0)] does not participate in the Bragg laser–driven dynamics. This owes to the wide momentum spread of our finite-sized condensate compared to the sharp spectral selectivity of our weak coupling fields [with a tunneling time of $\hbar/t = 511(22)$ μs]. To account for these deviations (detailed in the Supplementary Materials), we scale the predicted transmission curve by a factor of 0.48 with no extra offsets. This scaling better matches the lessened transmission near $\phi = 0$ but diverges from the data for larger values of flux where atoms should reflect off the boundary, regardless of the effects that hinder transmission.

We additionally investigate the full dynamics for the cases of homogeneous zero flux ($\phi = 0$) and maximally inhomogeneous flux ($\phi = \pi$), as shown in Fig. 3 (C and D). In both cases, we compare the complete momentum-state distributions to those predicted by Eq. 1 and extract the percentages of reflected and transmitted atoms. The calibrated tunneling rate for these data [$t/\hbar = 2\pi \times 344(21)$ Hz] differs from that of the variable flux data discussed above. The normalized integrated optical density (OD) plots for the $\phi = 0$ case in Fig. 3C show a significant percentage of the population leaving the four leftmost sites (denoted by white markers) and entering the rightmost sites (gray shaded markers). The number of transmitted atoms at times exceeds that of which remains in the four leftmost sites, as shown in the reflected and transmitted population dynamics at the bottom. These data qualitatively agree quite well with the theory predictions (with the same scaling as in Fig. 3B).

The observations of significant transmission for $\phi = 0$ are contrasted by our measurements for $\phi = \pi$, as shown in Fig. 3D. Here, in the upper OD plots, good qualitative agreement is found between the measured population dynamics and the unscaled theory predictions, with the population first leaving and then returning to the initial site (leftmost red marker). Although the $\phi = 0$ case showed limited transmission, in this $\phi = \pi$ case we observe significant reflection from the boundary. At the bottom, we see that the number of atoms in the four leftmost sites always significantly exceeds that of transmitted atoms. The theory curves have been scaled down to correct for the limited transmission near $\phi = 0$, so, in this case of maximal reflection, the scaling causes an underestimate of the transmitted fraction. This observation of reflection from a flux boundary, with the absence of any variation in the

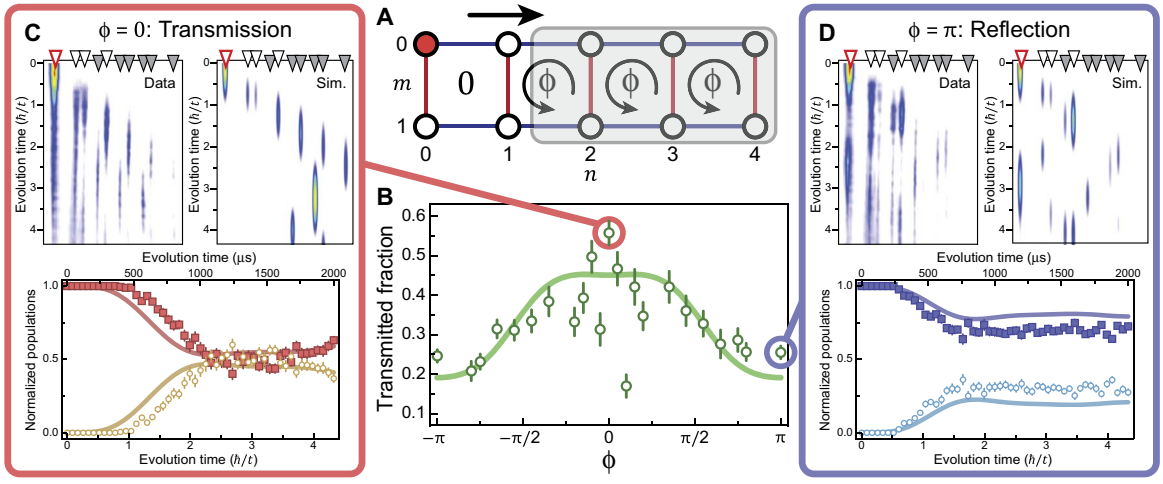

Fig. 3. Magnetic reflection. (**A**) Schematic depicting the lattice divided into two regions of different fluxes: 0 (unshaded, left) and ϕ (shaded, right). Population begins at the red filled-in lattice site. (**B**) Fraction of initial population transmitted into the shaded ϕ flux region as a function of ϕ after 1500-μs evolution time (~2.94 $\hbar/t$). Solid curve represents a numerical simulation with an overall scaling factor of 0.48 to fit the data. (**C** and **D**) Dynamics for (C) ϕ = 0 and (D) ϕ = π. Top: Integrated (over the image dimension normal to the lattice) OD images versus evolution time for data (left) and simulation (right, Sim). Leftmost red marker denotes initial site, and gray shaded markers denote shaded ϕ region. Bottom: Population in the zero-flux region (darker squares) and shaded ϕ region (open lighter circles) as a function of evolution time. Calibrated tunneling time [$\hbar/t$ = 462(28) μs] for these dynamics differs from that of (B), and solid simulation curves account for an identical scaling as in (B). All error bars denote 1 SE.

underlying potential energy landscape, is a purely quantum mechanical effect, in analogy to previous observations of quantum reflection (*27*).

CONCLUSION

Our capabilities to directly engineer artificial homogeneous and inhomogeneous gauge fields and directly image site populations in a synthetic lattice are extremely promising for future realizations of myriad model systems relevant to topology and transport. These include 2D models of localization at topological interfaces (*28*), in disordered quantum Hall systems, and in random gauge fields (*29*). Although our results are predominantly driven by single-particle physics, the condensate atoms in our momentum-space lattice have a long-ranged interaction, allowing for a straightforward extension to studies of interacting topological fluids. This could be accomplished through Feshbach-enhanced scattering properties, longer interrogation, and coherence times or by mapping to other forms of discrete motional eigenstates (trapped states instead of plane-wave momentum states) with a more local interaction (*30*) or internal spin states (*14*, *15*).

During the preparation of this manuscript, we became aware of two related works that have demonstrated spin-orbit coupling using transitions to long-lived excited states in optical lattice clocks (*31*, *32*), based on the synthetic dimensions scheme suggested by Wall *et al.* (*18*). In particular, using this technique, Livi *et al.* (*32*) has demonstrated a wide control of homogeneous artificial flux magnitudes in synthetic two-leg ladders.

MATERIALS AND METHODS

Experimental procedure

Our experiment began with the preparation of a ^{87}Rb Bose-Einstein condensate with ~5×10^4 atoms. We reached quantum degeneracy via all-optical evaporation in a trap composed of three optical dipole beams: two with a wavelength of 1064 nm and one with a wavelength of 1070 nm. Immediately following evaporation, the condensate was transferred to a trap mainly formed by one of these beams (wavelength λ_2 = 1064 nm). We then turned on a second beam (wavelength λ_1 = 781.5 nm) copropagating with this 1064-nm beam. At the same time, we switched on the acousto-optic modulators (AOMs) in our lattice setup, which allowed both the λ_1 and λ_2 beams to be retroreflected back toward the atoms, forming optical lattices.

The lattice setup, described in detail by Gadway (*23*) and Meier *et al.* (*24*), used AOMs to write specific frequencies onto the retro beam. These frequency components of the retroreflected beam were detuned from the single-frequency forward-propagating beam so as to resonantly address momentum-changing Bragg transitions of the atoms. Here, to extend our previously introduced scheme to two synthetic dimensions, we added an identical lattice AOM setup to control the additional lattice beam (wavelength λ_1), as shown in Fig. 1A. Figure 1B denotes where the states of the effective two-leg ladder lie on the atoms' free-particle dispersion relation. Here, the tall blue arrows denote a two-photon Bragg transition driven by the λ_2 beam that changes the momentum of a condensate at rest to $2\hbar k_2$ [site (0, 1)]. Similarly, the short red arrows denote a transition driven by the λ_1 beam that shifts the condensate from zero momentum to $2\hbar k_1$ [site (1, 0)]. We applied the specific frequency teeth shown in fig. S1C to the λ_1 (red, left) and λ_2 (blue, right) beams, thereby addressing transitions between and along the two legs of a 2×5 site ladder, respectively. By controlling the phases and amplitudes of these frequency components and their detunings from Bragg resonances, we could engineer arbitrary tunneling phases, tunneling amplitudes, and site energies. Here, although we had control over next–nearest-neighbor couplings relating to longer-range tunneling, we addressed only first-order Bragg transitions between nearest-neighbor states that differed by two-photon momentum.

The lasers addressed the atoms for some duration, during which a set of Bragg transitions were driven in a phase-, frequency-, and amplitude-controlled fashion. After this evolution time, during which the dynamics of an effective tight-binding Hamiltonian were realized (*23*, *24*), all the traps were turned off and the atoms fell for 18 ms of time of flight. The different momentum states of our condensate atoms separated during

time-of-flight, transverse to the direction of gravity, and the populations of the various orders were measured by absorption imaging, as in Fig. 1C.

Tunneling rate imbalance

The quoted tunneling rates for all experiments were averages of slightly unequal interleg and intraleg values. The ratios of interleg-to-intraleg tunneling for each data set were $t_y/t_x = 1.03 \pm 0.07$ for the shearing dynamics of Fig. 2B, $t_y/t_x = 0.93 \pm 0.05$ for the shearing versus flux data of Fig. 2D, $t_y/t_x = 0.83 \pm 0.07$ for the magnetic reflection versus flux data of Fig. 3B, and $t_y/t_x = 0.90 \pm 0.06$ for the magnetic reflection dynamics of Fig. 3 (C and D).

SUPPLEMENTARY MATERIALS

Supplementary material for this article is available at http://advances.sciencemag.org/cgi/content/full/3/4/e1602685/DC1

Supplementary Text

fig. S1. 2D lattice implementation.

fig. S2. Phase instability.

fig. S3. Nonzero initial shearing.

Reference (*33*)

REFERENCES AND NOTES

1. N. Goldman, J. C. Budich, P. Zoller, Topological quantum matter with ultracold gases in optical lattices. *Nat. Phys.* **12**, 639–645 (2016).
2. N. Gemelke, E. Sarajlic, Y. Bidel, S. Hong, S. Chu, Parametric amplification of matter waves in periodically translated optical lattices. *Phys. Rev. Lett.* **95**, 170404 (2005).
3. J. Struck, C. Ölschläger, M. Weinberg, P. Hauke, J. Simonet, A. Eckardt, M. Lewenstein, K. Sengstock, P. Windpassinger, Tunable gauge potential for neutral and spinless particles in driven optical lattices. *Phys. Rev. Lett.* **108**, 225304 (2012).
4. G. Jotzu, M. Messer, R. Desbuquois, M. Lebrat, T. Uehlinger, D. Greif, T. Esslinger, Experimental realization of the topological Haldane model with ultracold fermions. *Nature* **515**, 237–240 (2014).
5. D. Jaksch, P. Zoller, Creation of effective magnetic fields in optical lattices: The Hofstadter butterfly for cold neutral atoms. *New J. Phys.* **5**, 56 (2003).
6. M. Aidelsburger, M. Atala, S. Nascimbène, S. Trotzky, Y.-A. Chen, I. Bloch, Experimental realization of strong effective magnetic fields in an optical lattice. *Phys. Rev. Lett.* **107**, 255301 (2011).
7. H. Miyake, G. A. Siviloglou, C. J. Kennedy, W. C. Burton, W. Ketterle, Realizing the Harper Hamiltonian with laser-assisted tunneling in optical lattices. *Phys. Rev. Lett.* **111**, 185302 (2013).
8. A. L. Fetter, Rotating trapped Bose-Einstein condensates. *Rev. Mod. Phys.* **81**, 647–691 (2009).
9. J. Higbie, D. M. Stamper-Kurn, Periodically dressed Bose-Einstein condensate: A superfluid with an anisotropic and variable critical velocity. *Phys. Rev. Lett.* **88**, 090401 (2002).
10. I. B. Spielman, Raman processes and effective gauge potentials. *Phys. Rev. A* **79**, 063613 (2009).
11. J. Dalibard, F. Gerbier, G. Juzeliūnas, P. Öhberg, Artificial gauge potentials for neutral atoms. *Rev. Mod. Phys.* **83**, 1523–1543 (2011).
12. M. Genske, A. Rosch, Floquet-Boltzmann equation for periodically driven Fermi systems. *Phys. Rev. A* **92**, 062108 (2015).
13. S. Choudhury, E. J. Mueller, Stability of a Bose-Einstein condensate in a driven optical lattice: Crossover between weak and tight transverse confinement. *Phys. Rev. A* **92**, 063639 (2015).
14. O. Boada, A. Celi, J. I. Latorre, M. Lewenstein, Quantum simulation of an extra dimension. *Phys. Rev. Lett.* **108**, 133001 (2012).
15. A. Celi, P. Massignan, J. Ruseckas, N. Goldman, I. B. Spielman, G. Juzeliūnas, M. Lewenstein, Synthetic gauge fields in synthetic dimensions. *Phys. Rev. Lett.* **112**, 043001 (2014).
16. B. K. Stuhl, H.-I. Lu, L. M. Aycock, D. Genkina, I. B. Spielman, Visualizing edge states with an atomic Bose gas in the quantum Hall regime. *Science* **349**, 1514–1518 (2015).
17. M. Mancini, G. Pagano, G. Cappellini, L. Livi, M. Rider, J. Catani, C. Sias, P. Zoller, M. Inguscio, M. Dalmonte, L. Fallani, Observation of chiral edge states with neutral fermions in synthetic Hall ribbons. *Science* **349**, 1510–1513 (2015).
18. M. L. Wall, A. P. Koller, S. Li, X. Zhang, N. R. Cooper, J. Ye, A. M. Rey, Synthetic spin-orbit coupling in an optical lattice clock. *Phys. Rev. Lett.* **116**, 035301 (2016).
19. M.-S. Chang, Q. Qin, W. Zhang, L. You, M. S. Chapman, Coherent spinor dynamics in a spin-1 Bose condensate. *Nat. Phys.* **1**, 111–116 (2005).
20. F. L. Moore, J. C. Robinson, C. F. Bharucha, B. Sundaram, M. G. Raizen, Atom optics realization of the quantum δ-kicked rotor. *Phys. Rev. Lett.* **75**, 4598–4601 (1995).
21. J. Chabé, G. Lemarié, B. Grémaud, D. Delande, P. Szriftgiser, J. C. Garreau, Experimental observation of the Anderson metal-insulator transition with atomic matter waves. *Phys. Rev. Lett.* **101**, 255702 (2008).
22. B. Gadway, J. Reeves, L. Krinner, D. Schneble, Evidence for a quantum-to-classical transition in a pair of coupled quantum rotors. *Phys. Rev. Lett.* **110**, 190401 (2013).
23. B. Gadway, Atom-optics approach to studying transport phenomena. *Phys. Rev. A* **92**, 043606 (2015).
24. E. J. Meier, F. A. An, B. Gadway, Atom-optics simulator of lattice transport phenomena. *Phys. Rev. A* **93**, 051602 (2016).
25. E. J. Meier, F. A. An, B. Gadway, Observation of the topological soliton state in the Su–Schrieffer–Heeger model. *Nat. Commun.* **7**, 13986 (2016).
26. M. Atala, M. Aidelsburger, M. Lohse, J. T. Barreiro, B. Paredes, I. Bloch, Observation of chiral currents with ultracold atoms in bosonic ladders. *Nat. Phys.* **10**, 588–593 (2014).
27. T. A. Pasquini, M. Saba, G.-B. Jo, Y. Shin, W. Ketterle, D. E. Pritchard, T. A. Savas, N. Mulders, Low velocity quantum reflection of Bose-Einstein condensates. *Phys. Rev. Lett.* **97**, 093201 (2006).
28. T. H. Hsieh, H. Ishizuka, L. Balents, T. L. Hughes, Bulk topological proximity effect. *Phys. Rev. Lett.* **116**, 086802 (2016).
29. P. A. Lee, D. S. Fisher, Anderson localization in two dimensions. *Phys. Rev. Lett.* **47**, 882–885 (1981).
30. H. M. Price, T. Ozawa, N. Goldman, Synthetic dimensions for cold atoms from shaking a harmonic trap. *Phys. Rev. A* **95**, 023607 (2016).
31. S. Kolkowitz, S. L. Bromley, T. Bothwell, M. L. Wall, G. E. Marti, A. P. Koller, X. Zhang, A. M. Rey, J. Ye, Spin–orbit-coupled fermions in an optical lattice clock. *Nature* **542**, 66–70 (2017).
32. L. F. Livi, G. Cappellini, M. Diem, L. Franchi, C. Clivati, M. Frittelli, F. Levi, D. Calonico, J. Catani, M. Inguscio, L. Fallani, Synthetic dimensions and spin-orbit coupling with an optical clock transition. *Phys. Rev. Lett.* **117**, 220401 (2016).
33. J. Stenger, S. Inouye, A. P. Chikkatur, D. M. Stamper-Kurn, D. E. Pritchard, W. Ketterle, Bragg spectroscopy of a Bose-Einstein condensate. *Phys. Rev. Lett.* **82**, 4569–4573 (1999).

Acknowledgments: We thank S. Hegde, K. Padavić, I. Mondragon-Shem, S. Vishveshwara, and T. L. Hughes for helpful discussions, and J. O. Ang'ong'a for careful reading of the manuscript. **Author contributions:** F.A.A. and E.J.M. carried out the experiments. F.A.A. performed the data analysis. F.A.A. and B.G. wrote the manuscript. B.G. supervised the research. **Competing interests:** The authors declare that they have no competing interests. **Data and materials availability:** All data needed to evaluate the conclusions in the paper are present in the paper and/or the Supplementary Materials. Additional data related to this paper may be requested from the authors.

Submitted 31 October 2016
Accepted 24 February 2017
Published 21 April 2017
10.1126/sciadv.1602685

Citation: F. A. An, E. J. Meier, B. Gadway, Direct observation of chiral currents and magnetic reflection in atomic flux lattices. *Sci. Adv.* **3**, e1602685 (2017).